ACS APPLIED MATERIALS & INTERFACES

Research Article

www.acsami.org

Polymer-Enriched 3D Graphene Foams for Biomedical Applications

Jun Kit Wang,[†,‡,#] Gordon Minru Xiong,[§,#] Minmin Zhu,[§,⊥,∥] Barbaros Özyilmaz,[⊥,∥] Antonio Helio Castro Neto,[⊥,∥] Nguan Soon Tan,[▽,¶] and Cleo Choong*[,§,⊥]

[†]Residues and Resource Reclamation Centre (R3C), Nanyang Environment and Water Research Institute (NEWRI), Nanyang Technological University, 1 Cleantech Loop, Singapore 637141, Singapore

[‡]Interdisciplinary Graduate School and [§]School of Materials Science and Engineering, Nanyang Technological University, 50 Nanyang Avenue, Singapore 639798, Singapore

[⊥]Graphene Research Center, National University of Singapore, 6 Science Drive 2, Singapore 117546, Singapore

[∥]Department of Physics, National University of Singapore, Singapore 117542, Singapore

[▽]School of Biological Sciences, Nanyang Technological University, 60 Nanyang Avenue, Singapore 637551, Singapore

[¶]Institute of Molecular and Cell Biology, 61 Biopolis Drive, Proteos, A*STAR, Singapore 138673, Singapore

ABSTRACT: Graphene foams (GFs) are versatile nanoplatforms for biomedical applications because of their excellent physical, chemical, and mechanical properties. However, the brittleness and inflexibility of pristine GF (pGF) are some of the important factors restricting their widespread application. Here, a chemical-vapor-deposition-assisted method was used to synthesize 3D GFs, which were subsequently spin-coated with polymer to produce polymer-enriched 3D GFs with high conductivity and flexibility. Compared to pGF, both poly(vinylidene fluoride)-enriched GF (PVDF/GF) and polycaprolactone-enriched GF (PCL/GF) scaffolds showed improved flexibility and handleability. Despite the presence of the polymers, the polymer-enriched 3D GF scaffolds retained high levels of electrical conductivity because of the presence of microcracks that allowed for the flow of electrons through the material. In addition, polymer enrichment of GF led to an enhancement in the formation of calcium phosphate (Ca−P) compounds when the scaffolds were exposed to simulated body fluid. Between the two polymers tested, PCL enrichment of GF resulted in a higher in vitro mineralization nucleation rate because the oxygen-containing functional group of PCL had a higher affinity for Ca−P deposition and formation compared to the polar carbon−fluorine (C−F) bond in PVDF. Taken together, our current findings are a stepping stone toward future applications of polymer-enriched 3D GFs in the treatment of bone defects as well as other biomedical applications.

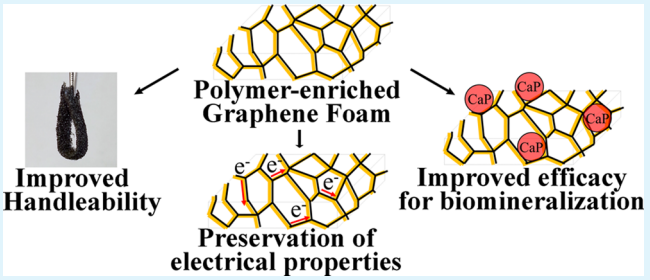

KEYWORDS: *graphene foam (GF), polycaprolactone (PCL), poly(vinylidene fluoride) (PVDF), chemical vapor deposition (CVD), biomineralization*

1. INTRODUCTION

An estimated 2.2 million bone replacement procedures are performed annually worldwide, making bone the second most transplanted human tissue after blood.[1−3] The current gold standard for bone transplant material is the use of autologous bone tissue isolated from the patient's own body. Because the drawbacks associated with bone autograft procedures include invasive surgical procedures, limited bone supply, and donor site morbidity,[4,5] alternative synthetic bone substitute materials have been investigated. However, because these bone substitute materials typically lack bioactive sites to promote bone formation, further surface modification processes, such as coating the surfaces of biomaterials with bonelike minerals of tricalcium phosphate (TCP) or hydroxyapatite (HA) to improve bioactivity and osteocompatibility, are required.[6−8]

As such, in vitro techniques that simulate the in vivo biomineralization process for forming the desired osteoconductive layer of complex minerals on the scaffold surfaces have been developed.[6,9] This biomimetic coating layer is commonly achieved by immersing the biomaterials in simulated body fluid (SBF), which has ionic concentrations similar to those of human blood plasma.[5] In such an environment, a natural self-assembly process will take place on the biomaterial surface. The efficacy of the biomaterial surface for supporting biomineralization, which is an indication of the bioactivity of the substrate,[10] can be investigated by observing the nucleation, growth, and phase transition of the resultant calcium phosphate (Ca−P) compounds. However, the rate of formation of Ca−P is highly dependent on the biomaterial's surface functional groups in affecting the absorption of calcium or phosphate ions.[11] Therefore, the surface functional groups on the biomaterial surface are crucial for substrate-controlled biomineralization.

Received: February 13, 2015
Accepted: March 30, 2015
Published: March 30, 2015

DOI: 10.1021/acsami.5b01440
ACS Appl. Mater. Interfaces 2015, 7, 8275−8283

It has previously been demonstrated that electrical stimulation also promotes bone formation because studies have shown increased osteoblast proliferation, overexpression of osteoblast markers in mesenchymal stem cells, and increased mineralization with the use of electrical stimulation.[12,13] In order to exploit the use of electrical stimuli for bone tissue engineering, implanted materials have to possess both electrical conductivity and biocompatibility. Hence, carbon-based materials such as 3D graphene foams (GFs) could be good candidates for biomedical applications. At present, most research on GFs is focused on the application of 3D structures in electronics and energy storage systems such as high-performance electromagnetic interference (EMI) and electrode materials because of their light weight and high electrical conductivity.[14,15] For energy storage applications, 3D hybrid GF structures have been used for asymmetric supercapacitors because their large 3D surface area allowed for the loading of electroactive materials.[16] However, limited research has been carried out on the development of 3D GFs for biomedical applications, despite the fact that recent studies on 3D GFs showed not only that are they biocompatible but also that the availability of large pores allowed for nutrient and waste exchange and tissue in-growth.[17,18] Their large internal 3D network can also potentially be used to increase the drug loading capacity,[19] while their excellent electrical and thermal properties make them a promising new class of smart scaffolding material for biomedical applications.[20]

In addition, earlier research has shown that the geometry of GF networks could promote osteogenic differentiation of human bone-marrow-derived mesenchymal stem cells as well as the growth and differentiation of neural stem cells (NSCs) into neurons.[18,21] In fact, excellent electrical coupling was observed between the 3D GFs and differentiated neurons as a result of the conductivity of the 3D GFs themselves.[18,22] However, the eventual clinical usage of 3D GFs is hampered by the fact that free-standing pristine 3D GF structures are very brittle, inflexible, and unsuitable for the manual handling necessary in a clinical setting. Therefore, in order for 3D GFs to be used for bone regeneration, both their ability to form an osteoconductive coating layer and their handleability would have to be improved without compromising their electrical properties.

3D GFs have previously been fabricated through chemical vapor deposition (CVD) on nickel (Ni) or copper foam templates, followed by the application of poly(methyl methacrylate) (PMMA) for support, and subsequent etching of the metal and removal of the polymer.[23,24] However, after metal etching and polymer removal, the remaining graphene layers, held in a 3D architecture, were very brittle, inflexible, and unsuitable for any manual handling necessary in biomedical applications. Therefore, in addition to optimizing their ability to form an osteoconductive coating layer, one needs to improve the handleability of these 3D GFs without compromising their electrical properties in order for these scaffolds to be effectively used for bone tissue engineering applications.

In the current study, two osteo-compatible polymers were introduced to the 3D graphene matrix after the CVD process, and the effects of polymer enrichment on the material properties and bone-binding ability of the formation of Ca−P deposition were investigated. Both poly(vinylidene fluoride) (PVDF) and polycaprolactone (PCL) have been used in a wide range of biomedical and bone tissue engineering applications because of their biocompatibility, favorable mechanical properties, and slow degradation rate in vivo.[25−29] Following the etching of the initial metal foam template, the resultant polymer-enriched 3D GFs were then exposed to 1× SBF to observe the biomineralization efficacy of these polymer-enriched 3D GFs.

2. MATERIALS AND METHODS

2.1. Materials. Nickel foams (5−120 pores/in.) were purchased from Latech Scientific Supply Pte. Ltd. (Singapore). Iron(III) chloride ($FeCl_3$; anhydrous, 98%) was purchased from Alfa Aesar (USA). Poly(vinylidene fluoride) (PVDF; average M_w 534000), polycaprolactone (PCL; average M_n 80000), *N*,*N*-dimethylformamide (DMF; anhydrous, 99.8%), calcium chloride dehydrate (≥99%), potassium phosphate dibasic trihydrate ($K_2HPO_4{\cdot}3H_2O$; ≥99%), sodium chloride (≥99.5%), sodium bicarbonate (≥99.7%), potassium chloride (99.0−100.5%), sodium sulfate (≥99.5%), and tris-(hydroxymethyl)aminomethane [$(CH_2OH)_3CNH_2$; ≥99.8%] were obtained from Sigma-Aldrich Chemical Co. (USA) and used without further purification. Chloroform (analytical reagent grade) was purchased from Fisher Scientific Co. (USA). Magnesium chloride hexahydrate was purchased from MP Biomedicals Australasia Pty Ltd. (Australia). Fuming 37% hydrochloric acid (HCl) was obtained from Merck KGaA (Germany). Epo-Tek H20E was obtained from Epoxy Technology Inc. (USA).

2.2. Fabrication of 3D GFs. 3D GFs were synthesized using CVD on Ni foam substrates following a previously established method.[23] The Ni foams were cut into 60 × 60 mm and placed in a quartz tube with an outer diameter of 100 mm and an inner diameter of 94 mm. They were heated to 1000 °C in a horizontal tube furnace under hydrogen with a 100 sccm gas flow and annealed for 5 min to clean their surfaces and to remove surface oxides. A small amount of methane gas (CH_4; 30 sccm) was then introduced into the reaction tube at 200 mTorr. The typical growth time was about 30 min, and the samples were rapidly cooled to room temperature under hydrogen gas (H_2; 200 sccm). Once the GF had been deposited onto the Ni, this Ni/GF substrate was then immersed in a 0.25 M $FeCl_3$) solution for 24 h to completely dissolve out the Ni foam to obtain a free-standing pristine GF (pGF) structure.

2.3. Fabrication of Polymer-Enriched 3D GFs. Polymer enrichment of GFs was carried out by modifying a previously published method of spin-coating PMMA onto Ni/GF for the conventional synthesis of free-standing GFs.[23] As shown schematically in Figure 1, the PVDF-enriched GF (PVDF/GF) scaffolds were fabricated by spin-coating Ni/GF at 600 rpm with a 5 wt % PVDF solution dissolved in DMF and then cured at 135 °C for 2 h in order to obtain the crystal ferroelectric structure. Similarly, the PCL-enriched GF (PCL/GF) scaffolds were fabricated by spin-coating Ni/GF at 600 rpm with a 9 wt % PCL solution dissolved in chloroform, followed by degassing in a DZF-6050 vacuum-drying oven (Shanghai Laboratory Instrument Work Co., Ltd., China) for 2 h, and thermally cured at 55 °C for 8 min. Finally, free-standing 3D PVDF/GF and PCL/GF structures were obtained by etching away the Ni in a 0.25 M $FeCl_3$ solution, followed by cleaning in distilled water and vacuum drying for further usage. Pristine PVDF (pPVDF) and pristine PCL (pPCL) scaffolds were used as control groups where the PVDF and PCL solutions were directly spin-coated onto a clean Ni foam at 600 rpm followed by thermal curing as described previously before

DOI: 10.1021/acsami.5b01440
ACS Appl. Mater. Interfaces 2015, 7, 8275−8283

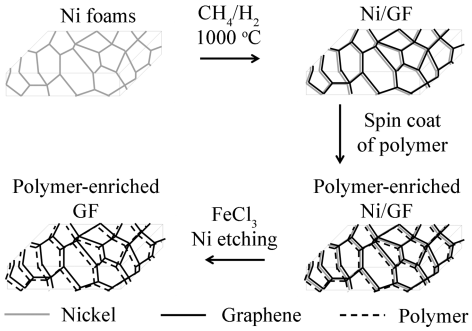

Figure 1. Schematic diagram of the processes involved in the synthesis of pristine 3D GF and subsequent polymer enrichment of the 3D GF structure.

etching out the Ni using 0.25 M $FeCl_3$. The pristine polymer scaffolds were then washed with distilled water and air-dried.

2.4. Pretreatment of 3D Pristine and Polymer-Enriched GFs. Graphene samples were cut into 10-mm-diameter circular shapes and pretreated by subjecting the samples to an alternating soak treatment process using a calcium- and phosphate-rich ion solution to form calcium and phosphate precursors prior to nucleation of Ca−P deposits in 1× SBF.[6,8] The samples were soaked in a 200 mM $CaCl_2$ solution for 10 min, followed by washing in distilled water for 5 min and then air drying for 15 min. The same set of samples was subsequently soaked in a 200 mM $K_2HPO_4{\cdot}3H_2O$ solution for 10 min, followed by washing in distilled water for 5 min and air drying for 15 min. For each sample, the alternating soak treatment was performed three times at room temperature.

2.5. Biomineralization of 3D Pristine and Polymer-Enriched GFs. The surface-modified samples were subsequently soaked in 5 mL of a 1× SBF solution at 37 °C and placed on an orbital shaker (Bibby Sterilin Ltd., U.K.) at 50 rpm for 2 weeks, where a fresh 1× SBF solution was replaced on a daily basis. The 1× SBF solution was prepared by dissolving reagent-grade Na^+ (142.0 mM), K^+ (5.0 mM), Mg^{2+} (1.5 mM), Ca^{2+} (2.5 mM), Cl^- (148.8 mM), HCO_3^- (4.2 mM), HPO_4^{2-} (1.0 mM), and SO_4^{2-} (0.5 mM) in distilled water.[8,30,31] The solution was buffered at pH 7.40 with $(CH_2OH)_3CNH_2$ and 1.0 M HCl. The samples were removed on days 1, 7, and 14, gently washed with two changes of distilled water, and then air-dried at room temperature for 24 h prior to further analyses.

2.6. Characterization of 3D Pristine and Polymer-Enriched 3D GFs. The morphology and microstructure of the scaffolds were characterized by scanning electron microscopy (SEM; JSM-6360F, JEOL Corp., Japan). The samples were coated with a thin layer of gold using a SPI Module sputter coater (SPI Supplies, USA) and imaged with an accelerating potential of 20 kV. The graphene structure was measured by a WITec CRM200 confocal Raman microscopy system (WITec Instruments Corp., Germany) performed at 488 nm, where the silicon peak was used as a reference for wavenumber calibration located at 521 cm^{-1}. The electrical conductivity of the scaffolds was determined by measuring their resistances using customized gold electrodes and a DMM 34450A digital multimeter (Agilent Technologies, USA). As shown in the representative setup in Figure 2, the scaffolds were cut into cylindrical shapes using a 7 mm leather belt hole puncher and a gold electrode was fashioned by sputtering gold for 2 min onto an aluminum disk (22 mm diameter) using a Emitech K575 sputtering coater

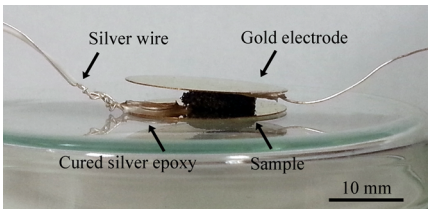

Figure 2. Electrical conductivity determined by sandwiching the scaffold between customized gold electrodes.

(Emitech, UK). A silver wire was fused to the gold electrode by application of biocompatible silver epoxy paste (Epo-Tek H20E), followed by 15 min of curing at 120 °C. The scaffold's resistivity, ρ (Ω·cm), was calculated from its measured resistance, R (Ω), using $\rho = RA/L$, where A is the cross-sectional area (cm^2) of the cylindrical scaffold and L (cm) is the height of the scaffold. The conductivity (S/cm) was then taken as the reciprocal of the resistivity.

For the postbiomineralization samples, SEM was used to observe the morphology and distribution of Ca−P deposits using the same conditions as those previously described. The functional groups of the polymers, the formation of Ca−P deposits, and its subsequent interaction with GF-based samples were further confirmed by Fourier transform infrared (FTIR; PerkinElmer instrument, USA) equipped with a Universal attenuated total reflection (ATR) at a resolution of 4 cm^{-1} in the range of 4000−650 cm^{-1} over 32 scans to identify the presence of PVDF and PCL on the polymer-enriched 3D GFs as well as the Ca−P-associated functional groups after biomineralization. The composition of the mineral phase was further determined by energy-dispersive X-ray (EDX) spectroscopy performed under the same condition as those of SEM analyses to obtain the calcium-to-phosphate (Ca/P) ratio (n = 10).

2.7. Statistical Analysis. All quantitative results are expressed as mean ± standard deviation. All experiments were carried out in triplicate unless otherwise specified, and statistical significance for conductivity measurements was determined using Kruskal−Wallis nonparametric one-way analysis of variance. A p value of less than 0.05 is considered to be statistically significant.

3. RESULTS AND DISCUSSION

3.1. Effect of Polymer Enrichment on the GF Morphology and Material Properties. Even though graphene is well-known for its intrinsic strength at the atomic level because of the strength of its covalent carbon bonds,[32] to our knowledge, the useful mechanical and handling properties of 3D GFs for biomedical application has never been demonstrated. If any substrate is to be used in a clinical setting, manual handling of the substrate directly or with a pair of tweezers should not result in unintentional compressive damage. As seen from Figure 3, a simple handling test with a pair of tweezers showed that the pGF substrate underwent visible compressive failure when held with a pair of tweezers (Figure 3a). However, the incorporation of polymers into the GF microarchitecture improved the scaffold handling ability, as observed in Figures 3d,e for the PVDF/GF and PCL/GF scaffolds, respectively. The spin-coated continuous polymer layers helped to enhance the handling ability of 3D GFs by improving the overall ductility of the 3D GFs, as observed from the good handling properties of the pPVDF (Figure 3b) and

DOI: 10.1021/acsami.5b01440
ACS Appl. Mater. Interfaces 2015, 7, 8275−8283

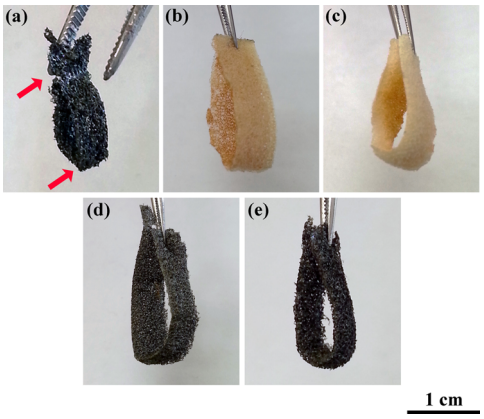

Figure 3. Optical images of the handleability of (a) pGF (arrows pointing to the fractured portions of the pGF), (b) pPVDF, (c) pPCL, (d) PVDF/GF, and (e) PCL/GF scaffolds when placed in a pair of tweezers.

pPCL (Figure 3c) scaffolds. Overall, the strengthening of the GF structures with polymers will make it possible to fabricate large-volume 3D conductive porous scaffolds that are nonbrittle and will be of practical use in a clinical setting.

The microstructural morphology and composition of pGF and polymer-enriched 3D GFs were analyzed using SEM and Raman spectroscopy. As seen from Figure 4a, the pGF sample had a wrinkled topography with flakelike structures observed. This wrinkled topography could have formed as the result of a difference in the thermal expansion coefficients between Ni and graphene when subjected to cooling during the synthesis process.[33] As a result of this wrinkled topography, mechanical interlocking of the polymer chains to the graphene surface will be improved during the spin-coating process because there is an increased surface area for interfacial adhesion and frictional forces between the polymer and graphene.[34,35] After the polymers were coated onto the pGF scaffold, a different surface morphology was observed compared that of to uncoated pGF. This surface morphology was also different from that of pristine polymer scaffolds of pPVDF (Figure 4b) and pPCL (Figure 4c). In the case of the PVDF/GF samples, flakelike structures could be observed on the coating surface, which are probably due to the formation of crystalline structures during the annealing process. On the other hand, this phenomenon was not observed for PCL/GF samples (Figure 4e) because only ripples that result in a wrinkled coating topography were observed because PCL is a semicrystalline polymer.

Raman spectroscopy was used to characterize the presence of graphene in the samples by looking at the relative intensity of the G and 2D bands. The resultant Raman spectrum (Figure 5)

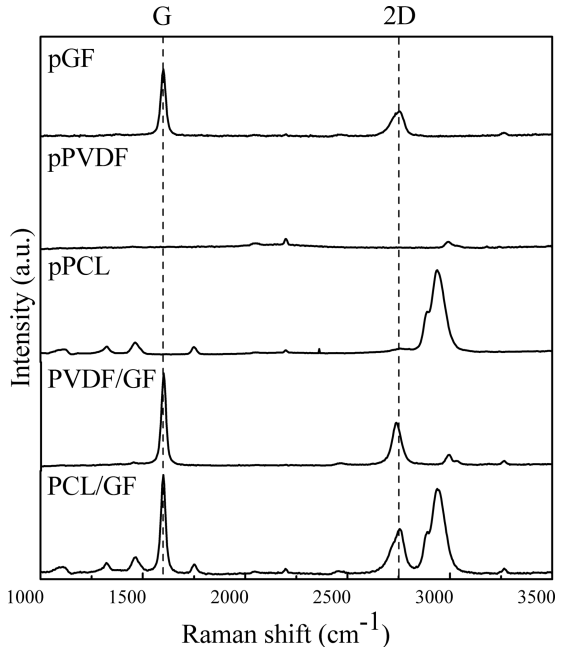

Figure 5. Raman spectra for different scaffolds with characteristic peaks corresponding to G and 2D bands for the scaffolds containing graphene.

showed the presence of characteristic peaks of graphene near 1580 and 2720 cm^{-1}, corresponding to the G and 2D bands, respectively. The small intensity of the D band at 1350 cm^{-1} is an indication of the high GF quality, while the high Raman intensity of the G band compared to that of the 2D band is characteristic of multilayered graphene. In the Raman spectrum

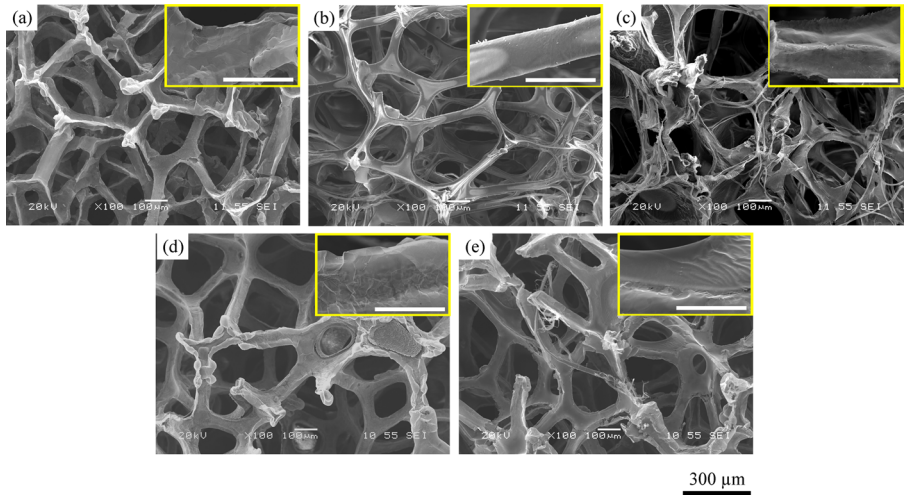

Figure 4. SEM images of the structure and morphology of the (a) pGF, (b) pPVDF, (c) pPCL, (d) PVDF/GF, and (e) PCL/GF scaffolds at 100× and 1000× magnification (inset: scale bar = 70 μm).

DOI: 10.1021/acsami.5b01440
ACS Appl. Mater. Interfaces 2015, 7, 8275−8283

of the PVDF/GF sample, the presence of graphene can be clearly identified by the presence of additional G and 2D peaks compared to pPVDF-associated peaks. The same was observed for the PCL/GF sample, where additional characteristic G and 2D peaks of graphene were also observed.

The electrical conductivities of the pGF and polymer-enriched GFs were measured by sandwiching the scaffolds between gold electrodes connected to a multimeter (Figure 2). Graphene macroassemblies reported in the literature have bulk electrical conductivities ranging from 1.0 S/cm for graphene "aerogels" to 5.0 × 10^{-3} S/cm for physical-cross-linked graphene sheets.[36] The electronic properties of few-layer graphene (FLG) grown using CVD were reported to be influenced by the stacking geometry between individual layers.[37] Localized stacking disorder may occur in multilayer CVD graphene, resulting in poorer electronic coupling between individual layers and, hence, compromised charge transport.[38] This was believed to be the case when using a challenging geometry for growth such as the 3D Ni foam in this paper with a calculated bulk conductivity of 0.36 ± 0.11 S/cm for pGF.

Despite the fact that both the PVDF/GF and PCL/GF scaffolds were enriched with nonconductive polymers, the bulk electrical conductivity was retained at 0.07 ± 0.02 and 0.14 ± 0.06 S/cm, respectively (Figure 6). This preservation of the

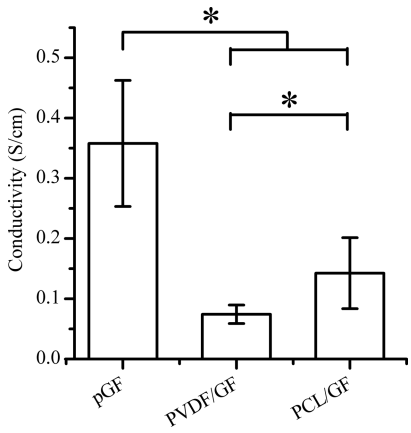

Figure 6. Average conductivity of the pGF and the hybrid scaffolds (PVDF/GF and PCL/GF) after polymer enrichment (*p < 0.05).

electrical conductivity could be due to the presence of "microcracks" in the polymer coatings, which could facilitate the flow of external electrons from the electrodes to the intact percolating network of the graphene microstructure. These "microcracks" were probably generated during the thermal curing process because heating and cooling of the polymer on the graphene substrate would result in residual stress-induced microfractures because the materials had different thermal expansion coefficients.[39]

The significantly higher (p < 0.05) electrical conductivity of PCL/GF compared to that of PVDF/GF could be due to differences in the crystallinity of the polymers themselves. While PCL is semicrystalline in nature, PVDF could be induced to form a ferroelectric crystalline phase during the annealing process at 135 °C for 2 h.[40] As a consequence of the annealing-induced crystalline phase and structural rearrangement of the PVDF coating, the fracture behavior of PVDF differs from that of PCL. This subsequently leads to a PVDF coating with less microcrack formation (Figure 4b) that resulted in PVDF/GF having better insulative properties than PCL/GF.[40]

Further characterization using FTIR analysis showed the presence of distinct peaks of graphene and the functional groups (Figure 7). Overall, pGF mainly consists of carbon

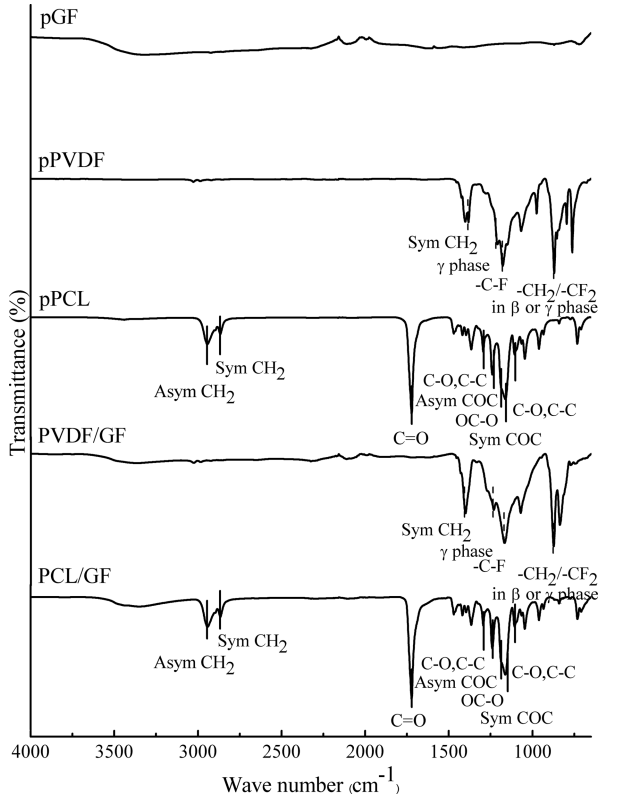

Figure 7. ATR-FTIR analysis of the pGF and hybrid scaffolds where fluorine-containing functional groups of PVDF observed in both pPVDF and PVDF/GF are indicated by the dashed lines and carbonyl functional groups of PCL present in both pPCL and PCL/GF are indicated by the solid lines.

double bonds, and thus random peaks were observed with a poor baseline. At the same time, graphene can easily adsorb and desorb various atoms or molecules such as hydroxyl (OH^-) groups, and thus a broad peak near 3300 cm^{-1} can be observed from the spectra. For the pristine polymers and polymer-enriched 3D GFs, the characteristic peaks of PVDF and PCL were present, as indicated by the C−H rocking with C−F stretching in PVDF (840 cm^{-1}) and the carbonyl stretching and aliphatic groups (2947 and 2865 cm^{-1}) of PCL. The presence of the peaks at 840 and 1276 cm^{-1} in the PVDF spectrum indicates that PVDF is mainly β-phase with excellent crystallinity after the annealing process.[41−43] However, the presence of graphene in both types of polymer-enriched 3D GFs is hardly detectable by FTIR because the aromatic vibration of graphene is weak.

3.2. In Vitro Biomineralization Studies. In order to assess the bioactivity and potential of these scaffolds for bone application, in vitro biomineralization studies were conducted using 1× SBF to mimic the biomineralization process in natural bone. The bone-binding ability and rate of nucleation and growth of Ca−P deposits are indicators of a material's osteoconductivity.[44−46] In general, the formation of Ca−P crystals begins with aggregation of the Ca−P prenucleation clusters, followed by densification of these clusters into amorphous Ca−P and, even later, their transformation into

DOI: 10.1021/acsami.5b01440
ACS Appl. Mater. Interfaces 2015, 7, 8275−8283

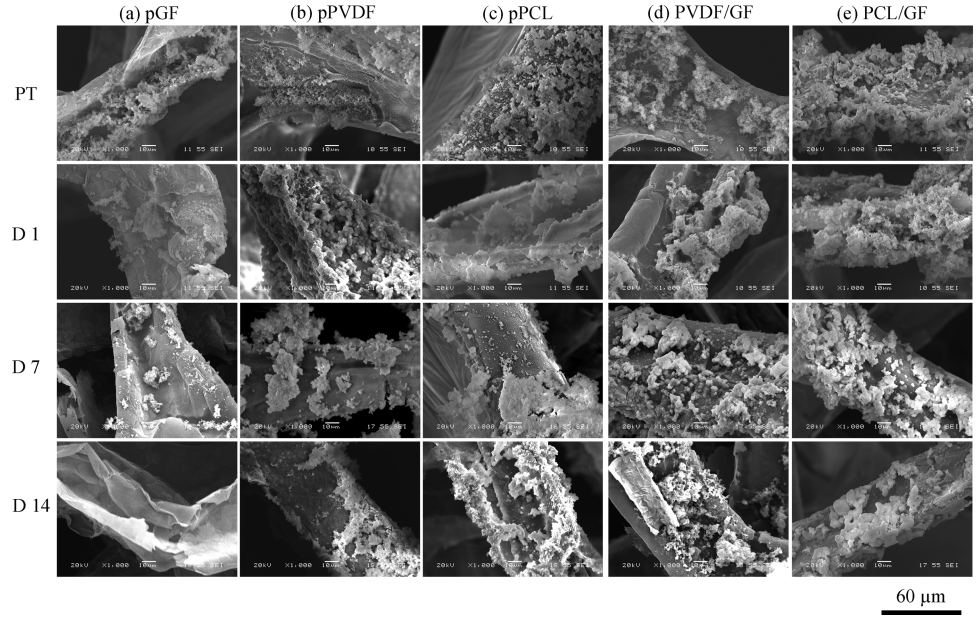

Figure 8. SEM images showing the formation and distribution of Ca−P on the 3D pGF and hybrid scaffolds at different time points. PT: pretreatment. D 1: Day 1. D 7: Day 7. D 14: Day 14.

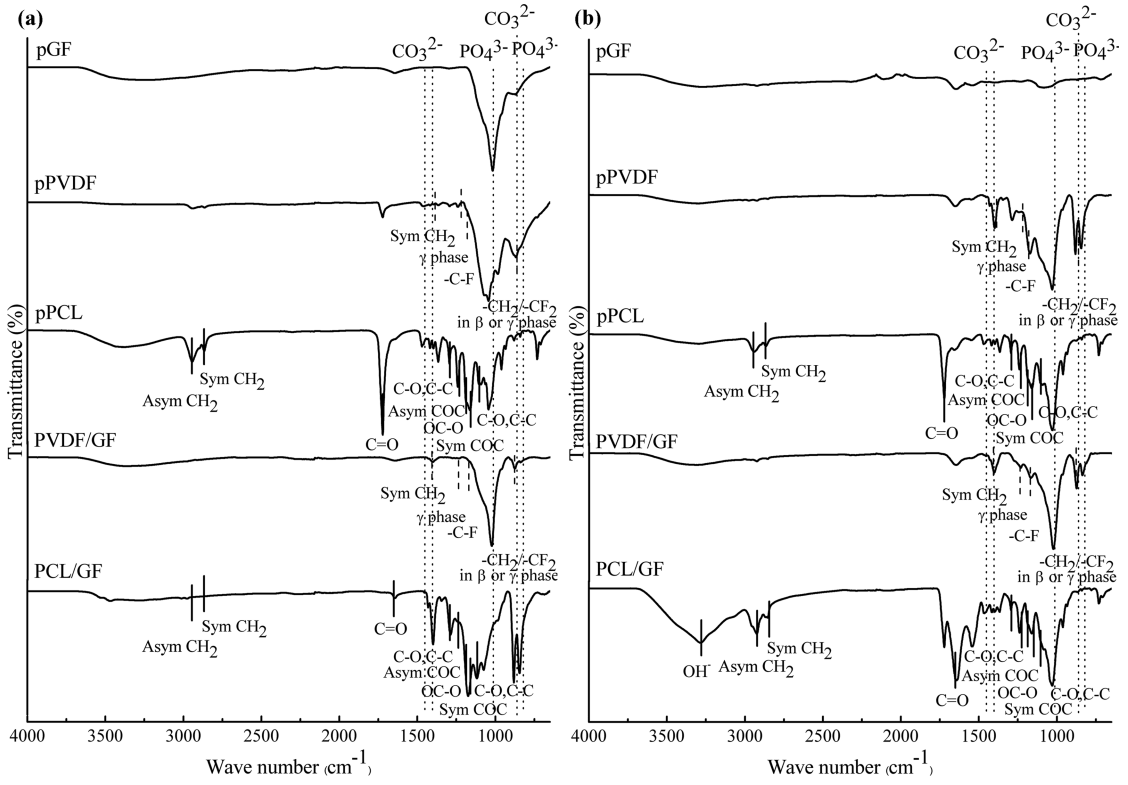

Figure 9. ATR-FTIR analyses of the different scaffolds after (a) pretreatment and (b) 14 days of immersion in 1× SBF with characteristic peaks for the mineral phases of the carbonate and phosphate functional groups (dotted lines) and the fluorine-containing functional groups (dashed lines) of PVDF and the carbonyl functional groups of PCL (solid lines).

crystalline apatite.[47] From the SEM images (Figure 8), it was observed that, after the pretreatment (PT) process, there was even nucleation of Ca−P deposits on all of the different groups of samples after alternating soak treatments in calcium- and phosphate-rich solutions. However, in the case of the pGF sample (Figure 8a), a decreased amount of the Ca−P deposits was observed compared to the other sample groups because of detachment or dissolution of the deposits from the graphene surface. This suggests that the Ca−P deposits on pGF were not stable prenucleation clusters because they could easily be dissociated from the pGF surface.

However, in the case of the polymer-enriched 3D GFs (Figure 8d,e), an increase in finely dispersed Ca−P deposits was observed throughout the 3D scaffold network from days 1

DOI: 10.1021/acsami.5b01440
ACS Appl. Mater. Interfaces 2015, 7, 8275−8283

Table 1. Ca/P Ratios Obtained by SEM−EDX for the Different Groups of Scaffolds

	pretreatment	day 1	day 7	day 14
pGF	0.987 ± 0.114	1.095 ± 0.076	1.561 ± 0.443	0.398 ± 0.121
pPVDF	0.873 ± 0.197	0.958 ± 0.076	1.270 ± 0.175	1.389 ± 0.512
pPCL	1.165 ± 0.626	1.260 ± 0.207	1.592 ± 0.823	1.544 ± 0.846
PVDF/GF	0.947 ± 0.041	1.275 ± 0.235	1.197 ± 0.089	1.491 ± 0.571
PCL/GF	0.861 ± 0.092	1.608 ± 0.612	1.210 ± 0.148	1.460 ± 0.504

to 14. Thus, the incorporation of both PVDF and PCL into the GF had stabilized the formation of Ca−P deposits. This phenomenon could be attributed to the polar carbon−fluorine (C−F) bonds of PVDF and oxygen-containing functional groups in PCL, which could anchor the deposition of Ca−P prenucleation clusters during pretreatment, and subsequently led to the growth and formation of stable Ca−P deposits.[30,47] Compared to PVDF-enriched samples, the PCL/GF samples had a denser Ca−P coverage even after just 1 day of exposure to a 1× SBF solution, which could be due to stronger interactions between the electronegative oxygen atoms and the positively charged calcium ions (Ca^{2+}) on PCL compared to the interactions between the ions and polar fluoride groups on PVDF.[11] Conversely, less Ca−P deposits were observed for the pPVDF and pPCL samples (Figure 8b,c). This observation is similar to those reported by others showing that pristine, unmodified polymers have a slower growth rate of Ca−P.[9,11,31]

The differences in the distribution of Ca−P deposits could also be due to the different surface topographies of the samples because a higher surface roughness could facilitate the aggregation of Ca−P prenucleation clusters, as well as promote the growth and mechanical attachment of Ca−P deposits.[48,49] In the case of the chemically inert pGF, the Ca−P deposits were probably physically held in place by the wrinkled rough surface. However, because they were not chemically bonded to the surface, they eventually detached over time. For the formation of Ca−P deposits on pPVDF and pPCL, chemical interactions between the functional groups of the polymers and Ca−P prenucleation clusters would still take place despite their relatively smooth surfaces (Figure 4b,c). Hence, the polymer-enriched substrates (PVDF/GF and PCL/GF) could have benefited from the combinatory effect of both chemically and mechanically driven Ca−P growth, which is the result of the presence of functional groups on the polymers, as well as the rough surface coating from the wrinkled GF substrate. This ultimately led to a denser distribution of Ca−P deposits on the polymer-enriched substrates compared to all other substrates.

3.3. Characterization of Ca−P Compounds. The formation of Ca−P deposits on the 3D scaffolds was further verified by FTIR, and the Ca/P ratios of the mineral deposits were analyzed by SEM−EDX. The resultant FTIR spectra of pretreated samples (Figure 9a) and the samples after 14 days of immersion in 1× SBF (Figure 9b) showed the presence of characteristic peaks of Ca−P deposits around 840, 874, 1028, 1418, and 1470 cm^{-1}, which correspond to the carbonate and phosphate groups. The presence of peaks near 874 cm^{-1} and the region of 1418−1470 cm^{-1} could be attributed to the carbonate groups (CO_3^{2-}), while the phosphate peaks (PO_4^{3-}) were observed near 840 and 1028 cm^{-1}.[50−52] In fact, after the initial alternating soak pretreatment process, all of the different groups of scaffolds already contained phosphate peaks (Figure 9a). This is in agreement with the pretreated SEM images (Figure 8, PT) showing fine mineral deposits on all of the pretreated scaffolds. However, in the case of the pGF substrate, the height of the phosphate peaks decreased with increasing immersion time in 1× SBF over 14 days (Figure 9b), suggesting that there was a loss of crystallinity due to Ca−P dissolution over time. On the other hand, strong phosphate peaks were still observed even after 14 days for the pristine polymer scaffolds and the polymer-enriched 3D GFs, which could be an indication of stably nucleated Ca−P deposits on those scaffolds when exposed to 1× SBF. However, over 14 days of mineralization, only the PCL/GF scaffolds exhibited a $-OH^-$ peak near 3286 cm^{-1}, which typically belongs to the $-OH^-$ group in the c column of the HA lattice. This suggests that the PCL/GF scaffold could potentially be able to promote the formation of HA specifically.

Further analysis by SEM−EDX was carried out to compare the Ca/P ratios of the different scaffold groups. As seen from Table 1, all of the Ca−P deposits had low Ca/P ratios of close to 1.00 after the pretreatment process. After the samples were immersed in the 1× SBF solution, subsequent nucleation and growth processes led to an increase in the Ca/P ratios with increasing soak time. The high Ca/P ratio observed on day 1 for PCL/GF, which could be explained by the initial strong interaction of Ca^{2+} ions with the carbonyl functional groups in the PCL, led to the formation of unstable clusters, which were stabilized over 14 days in 1× SBF. At day 14, all of the scaffolds, except for pGF, where the Ca−P deposition was not stable, had Ca/P ratios in a range of 1.4−1.5, which suggests the formation of TCP or calcium-deficient HA. This is in accordance with findings by other groups that the Ca−P formed in SBF is that of calcium-deficient carbonated HA.[9,53] In general, polymer enrichment of 3D GFs helped to increase the nucleation and growth rate of the Ca−P deposits and provided the necessary functional groups for retaining the Ca−P deposits. Also, the presence of the oxygen-containing functional group of PCL resulted in a higher nucleation rate of the Ca−P deposits compared to PVDF. Thus, PCL enrichment of GF could lead to better osteoconductivity.

4. CONCLUSION

Overall, it was found that polymer enrichment of GFs led to an improvement in the handling ability and flexibility compared to that of pGF. In addition, polymer incorporation resulted in stabilization of Ca−P nucleation and allowed for the growth of Ca−P compounds. In contrast, pPVDF and pPCL scaffolds showed minimal Ca−P nucleation and growth. Moreover, growth of the Ca−P deposits occurred throughout the scaffold microarchitecture, which suggests that GF plays an important role as a template for the nucleation and oriented growth of Ca−P deposits. Overall, the 3D PCL/GF is a promising scaffold for bone-related applications because it demonstrated the fastest biomineralization rate (i.e., within 1 day) and the presence of a hydroxyl group in the Ca−P deposits. In addition, retention of the electrical properties would allow for the development of an electroactive scaffold that is able to further contribute to bone formation and healing.

DOI: 10.1021/acsami.5b01440
ACS Appl. Mater. Interfaces 2015, 7, 8275−8283

AUTHOR INFORMATION

Corresponding Author

*Telephone: 65 6513 8166. E-mail: cleochoong@ntu.edu.sg.

Author Contributions

The manuscript was written through contributions of all authors. All authors have given approval to the final version of the manuscript.

Author Contributions

#These authors contributed equally.

Funding

The authors are grateful for research scholarships from Nanyang Environment and Water Research Institute/Interdisciplinary Graduate School, Nanyang Technological University, Singapore (NEWRI/IGS), and the Economic Development Board (EDB) of Singapore. They would also like to acknowledge funding support from the Ministry of Education (MoE) Academic Research Fund (AcRF) Tier1 Funding (RG52/13).

Notes

The authors declare no competing financial interest.

ACKNOWLEDGMENTS

This research is supported by the National Research Foundation, Prime Minister's Office, Singapore, under its Medium Sized Centre Programme. The electron microscopy work was performed at the Facility for Analysis, Characterization, Testing and Simulation at Nanyang Technological University, Singapore.

ABBREVIATIONS

GF, graphene foam
pGF, pristine graphene foam
PCL, polycaprolactone
PVDF, poly(vinylidene fluoride)
pPCL, pristine polycaprolactone
pPVDF, pristine poly(vinylidene fluoride)
PCL/GF, polycaprolactone-enriched graphene foams
PVDF/GF, poly(vinylidene fluoride)-enriched graphene foams
CVD, chemical vapor deposition
SBF, simulated body fluid
PMMA, poly(methyl methacrylate)
Ni, nickel
CH_4, methane gas
H_2, hydrogen gas
$FeCl_3$, iron(III) chloride
SEM, scanning electron microscopy
EDX, energy-dispersive X-ray
FTIR, Fourier transform infrared
ATR, attenuated total reflection
$CaCl_2$, calcium chloride
$K_2HPO_4{\cdot}3H_2O$, potassium phosphate dibasic trihydrate
HCl, hydrochloric acid
CO_3^{2-}, carbonate
PO_4^{3-}, phosphate
OH^-, hydroxyl
C−F, carbon−fluorine
TCP, tricalcium phosphate
HA, hydroxyapatite
Ca−P, calcium phosphate
EMI, electromagnetic interference
NSCs, neural stem cells
FLG, few-later graphene
PT, pretreatment

REFERENCES

(1) Wong, H. M.; Chu, P. K.; Leung, F. K. L.; Cheung, K. M. C.; Luk, K. D. K.; Yeung, K. W. K. Engineered Polycaprolactone−Magnesium Hybrid Biodegradable Porous Scaffold for Bone Tissue Engineering. *Prog. Nat. Sci.: Mater. Int.* **2014**, *24*, 561−567.

(2) Cunha, M. J. S.; Esper, L. A.; Sbrana, M. C.; de Oliveira, P. G. F. P.; do Valle, A. L.; de Almeida, A. L. P. F. Effect of Low-Level Laser on Bone Defects Treated with Bovine or Autogenous Bone Grafts: In Vivo Study in Rat Calvaria. *BioMed. Res. Int.* **2014**, *2014*, 104230−1−104230−9.

(3) Binte Atique, F.; Rahman Khalil, M. M. The Bacterial Contamination of Allogeneic Bone and Emergence of Multidrug-Resistant Bacteria in Tissue Bank. *BioMed. Res. Int.* **2014**, *2014*, 430581−1−430581−5.

(4) Silber, J. S.; Anderson, D. G.; Daffner, S. D.; Brislin, B. T.; Leland, J. M.; Hilibrand, A. S.; Vaccaro, A. R.; Albert, T. J. Donor Site Morbidity After Anterior Iliac Crest Bone Harvest for Single-Level Anterior Cervical Discectomy and Fusion. *Spine* **2003**, *28*, 134−139.

(5) Schwartz, C.; Martha, J.; Kowalski, P.; Wang, D.; Bode, R.; Li, L.; Kim, D. Prospective Evaluation of Chronic Pain Associated with Posterior Autologous Iliac Crest Bone Graft Harvest and Its Effect on Postoperative Outcome. *Health Qual. Life Outcomes* **2009**, *7*, 49−1−49−9.

(6) Oyane, A.; Uchida, M.; Yokoyama, Y.; Choong, C.; Triffitt, J.; Ito, A. Simple Surface Modification of Poly(Epsilon-Caprolactone) to Induce Its Apatite-Forming Ability. *J. Biomed. Mater. Res., Part A* **2005**, *75*, 138−145.

(7) Kokubo, T.; Kushitani, H.; Sakka, S.; Kitsugi, T.; Yamamuro, T. Solutions Able to Reproduce In Vivo Surface-Structure Changes in Bioactive Glass-Ceramic A-W. *J. Biomed. Mater. Res.* **1990**, *24*, 721−734.

(8) Oyane, A.; Uchida, M.; Choong, C.; Triffitt, J.; Jones, J.; Ito, A. Simple Surface Modification of Poly(ε-Caprolactone) for Apatite Deposition from Simulated Body Fluid. *Biomaterials* **2005**, *26*, 2407−2413.

(9) Bose, S.; Tarafder, S. Calcium Phosphate Ceramic Systems in Growth Factor and Drug Delivery for Bone Tissue Engineering: A Review. *Acta Biomater.* **2012**, *8*, 1401−1421.

(10) Tao, J. FTIR and Raman Studies of Structure and Bonding in Mineral and Organic-Mineral Composites. *Methods Enzymol.* **2013**, *532*, 533−556.

(11) Li, X.; Lan, J.; Ai, M.; Guo, Y.; Cai, Q.; Yang, X. Biomineralization on Polymer-Coated Multi-Walled Carbon Nanotubes with Different Surface Functional Groups. *Colloids Surf., B* **2014**, *123*, 753−761.

(12) Meng, S.; Rouabhia, M.; Zhang, Z. Electrical Stimulation Modulates Osteoblast Proliferation and Bone Protein Production through Heparin-Bioactivated Conductive Scaffolds. *Bioelectromagnetics* **2013**, *34*, 189−199.

(13) Creecy, C. M.; O'Neill, C. F.; Arulanandam, B. P.; Sylvia, V. L.; Navara, C. S.; Bizios, R. Mesenchymal Stem Cell Osteodifferentiation in Response to Alternating Electric Current. *Tissue Eng., Part A* **2013**, *19*, 467−474.

(14) Chen, Z.; Xu, C.; Ma, C.; Ren, W.; Cheng, H. M. Lightweight and Flexible Graphene Foam Composites for High-Performance Electromagnetic Interference Shielding. *Adv. Mater.* **2013**, *25*, 1296−1300.

(15) Luo, J.; Liu, J.; Zeng, Z.; Ng, C. F.; Ma, L.; Zhang, H.; Lin, J.; Shen, Z.; Fan, H. J. Three-Dimensional Graphene Foam Supported Fe_3O_4 Lithium Battery Anodes with Long Cycle Life and High Rate Capability. *Nano Lett.* **2013**, *13*, 6136−6143.

(16) Liu, J.; Zhang, L.; Wu, H. B.; Lin, J.; Shen, Z.; Lou, X. W. High-performance Flexible Asymmetric Supercapacitors Based on a New

DOI: 10.1021/acsami.5b01440
ACS Appl. Mater. Interfaces 2015, 7, 8275−8283

Graphene Foam/Carbon Nanotube Hybrid Film. *Energy Environ. Sci.* **2014**, *7*, 3709−3719.
(17) Yin, S.; Wu, Y.-L.; Hu, B.; Wang, Y.; Cai, P.; Tan, C. K.; Qi, D.; Zheng, L.; Leow, W. R.; Tan, N. S.; Wang, S.; Chen, X. Three-Dimensional Graphene Composite Macroscopic Structures for Capture of Cancer Cells. *Adv. Mater. Interfaces* **2014**, *1*, 1300043−1−1300043−6.
(18) Li, N.; Zhang, Q.; Gao, S.; Song, Q.; Huang, R.; Wang, L.; Liu, L.; Dai, J.; Tang, M.; Cheng, G. Three-Dimensional Graphene Foam as a Biocompatible and Conductive Scaffold for Neural Stem Cells. *Sci. Rep.* **2013**, *3*, 1604−1−1604−6.
(19) Bressan, E.; Ferroni, L.; Gardin, C.; Sbricoli, L.; Gobbato, L.; Ludovichetti, F. S.; Tocco, I.; Carraro, A.; Piattelli, A.; Zavan, B. Graphene Based Scaffolds Effects on Stem Cells Commitment. *J. Transl. Med.* **2014**, *12*, 296−1−296−15.
(20) Jia, J.; Sun, X.; Lin, X.; Shen, X.; Mai, Y.-W.; Kim, J.-K. Exceptional Electrical Conductivity and Fracture Resistance of 3D Interconnected Graphene Foam/Epoxy Composites. *ACS Nano* **2014**, *8*, 5774−5783.
(21) Crowder, S. W.; Prasai, D.; Rath, R.; Balikov, D. A.; Bae, H.; Bolotin, K. I.; Sung, H. J. Three-Dimensional Graphene Foams Promote Osteogenic Differentiation of Human Mesenchymal Stem Cells. *Nanoscale* **2013**, *5*, 4171−4176.
(22) Song, Q.; Jiang, Z.; Li, N.; Liu, P.; Liu, L.; Tang, M.; Cheng, G. Anti-Inflammatory Effects of Three-Dimensional Graphene Foams Cultured with Microglial Cells. *Biomaterials* **2014**, *35*, 6930−6940.
(23) Cao, X.; Shi, Y.; Shi, W.; Lu, G.; Huang, X.; Yan, Q.; Zhang, Q.; Zhang, H. Preparation of Novel 3D Graphene Networks for Supercapacitor Applications. *Small* **2011**, *7*, 3163−3168.
(24) Chen, Z.; Ren, W.; Gao, L.; Liu, B.; Pei, S.; Cheng, H. M. Three-Dimensional Flexible and Conductive Interconnected Graphene Networks Grown by Chemical Vapour Deposition. *Nat. Mater.* **2011**, *10*, 424−428.
(25) Ródenas-Rochina, J.; Ribelles, J.; Lebourg, M. Comparative Study of PCL-HAp and PCL-Bioglass Composite Scaffolds for Bone Tissue Engineering. *J. Mater. Sci.: Mater. Med.* **2013**, *24*, 1293−1308.
(26) Binulal, N. S.; Natarajan, A.; Menon, D.; Bhaskaran, V. K.; Mony, U.; Nair, S. V. PCL−Gelatin Composite Nanofibers Electrospun using Diluted Acetic Acid−Ethyl Acetate Solvent System for Stem Cell-Based Bone Tissue Engineering. *J. Biomater. Sci., Polym. Ed.* **2013**, *25*, 325−340.
(27) Yuan, S.; Xiong, G.; Wang, X.; Zhang, S.; Choong, C. Surface Modification of Polycaprolactone Substrates using Collagen-Conjugated Poly(Methacrylic Acid) Brushes for the Regulation of Cell Proliferation and Endothelialisation. *J. Mater. Chem. B* **2012**, *22*, 13039−13049.
(28) Xiong, G. M.; Yuan, S.; Tan, C. K.; Wang, J. K.; Liu, Y.; Yang Tan, T. T.; Tan, N. S.; Choong, C. Endothelial Cell Thrombogenicity is Reduced by ATRP-Mediated Grafting of Gelatin onto PCL Surfaces. *J. Mater. Chem. B* **2014**, *2*, 485−493.
(29) Damaraju, S. M.; Wu, S.; Jaffe, M.; Arinzeh, T. L. Structural Changes in PVDF Fibers due to Electrospinning and Its Effect on Biological Function. *Biomed. Mater.* **2013**, *8*, 045007−1−045007−11.
(30) Oyane, A.; Uchida, M.; Yokoyama, Y.; Choong, C.; Triffitt, J.; Ito, A. Simple Surface Modification of Poly(ε-Caprolactone) to Induce Its Apatite-Forming Ability. *J. Biomed. Mater. Res., Part A* **2005**, *75A*, 138−145.
(31) Choong, C.; Yuan, S.; Thian, E. S.; Oyane, A.; Triffitt, J. Optimization of Poly(ε-Caprolactone) Surface Properties for Apatite Formation and Improved Osteogenic Stimulation. *J. Biomed. Mater. Res., Part A* **2012**, *100A*, 353−361.
(32) Lee, C.; Wei, X.; Kysar, J. W.; Hone, J. Measurement of the Elastic Properties and Intrinsic Strength of Monolayer Graphene. *Science* **2008**, *321*, 385−388.
(33) Chae, S. J.; Güneş, F.; Kim, K. K.; Kim, E. S.; Han, G. H.; Kim, S. M.; Shin, H.-J.; Yoon, S.-M.; Choi, J.-Y.; Park, M. H.; Yang, C. W.; Pribat, D.; Lee, Y. H. Synthesis of Large-Area Graphene Layers on Poly-Nickel Substrate by Chemical Vapor Deposition: Wrinkle Formation. *Adv. Mater.* **2009**, *21*, 2328−2333.
(34) Ramakrishna, S. N.; Espinosa-Marzal, R. M.; Naik, V. V.; Nalam, P. C.; Spencer, N. D. Adhesion and Friction Properties of Polymer Brushes on Rough Surfaces: A Gradient Approach. *Langmuir* **2013**, *29*, 15251−15259.
(35) Nadkarni, P. D.; Kildsig, D. O.; Kramer, P. A.; Banker, G. S. Effect of Surface Roughness and Coating Solvent on Film Adhesion to Tablets. *J. Pharm. Sci.* **1975**, *64*, 1554−1557.
(36) Worsley, M. A.; Pauzauskie, P. J.; Olson, T. Y.; Biener, J.; Satcher, J. H.; Baumann, T. F. Synthesis of Graphene Aerogel with High Electrical Conductivity. *J. Am. Chem. Soc.* **2010**, *132*, 14067−14069.
(37) Latil, S.; Henrard, L. Charge Carriers in Few-Layer Graphene Films. *Phys. Rev. Lett.* **2006**, *97*, 036803−1−036803−4.
(38) Reina, A.; Jia, X.; Ho, J.; Nezich, D.; Son, H.; Bulovic, V.; Dresselhaus, M. S.; Kong, J. Large Area, Few-Layer Graphene Films on Arbitrary Substrates by Chemical Vapor Deposition. *Nano Lett.* **2008**, *9*, 30−35.
(39) Fang, W.; Lo, C.-Y. On the Thermal Expansion Coefficients of Thin Films. *Sens. Actuators, A* **2000**, *84*, 310−314.
(40) Wallner, G. M.; Major, Z.; Maier, G. A.; Lang, R. W. Fracture Analysis of Annealed PVDF Films. *Polym. Test.* **2008**, *27*, 392−402.
(41) Elzubair, A.; Elias, C. N.; Suarez, J. C. M.; Lopes, H. P.; Vieira, M. V. B. The Physical Characterization of a Thermoplastic Polymer for Endodontic Obturation. *J. Dent.* **2006**, *34*, 784−789.
(42) Salimi, A.; Yousefi, A. A. Analysis Method: FTIR Studies of β-Phase Crystal Formation in Stretched PVDF Films. *Polym. Test.* **2003**, *22*, 699−704.
(43) Sandoval, S.; Kumar, N.; Sundaresan, A.; Rao, C. N.; Fuertes, A.; Tobias, G. Enhanced Thermal Oxidation Stability of Reduced Graphene Oxide by Nitrogen Doping. *Chem.—Eur. J.* **2014**, *20*, 11999−12003.
(44) Cui, W.; Li, X.; Chen, J.; Zhou, S.; Weng, J. In Situ Growth Kinetics of Hydroxyapatite on Electrospun Poly(DL-lactide) Fibers with Gelatin Grafted. *Cryst. Growth Des.* **2008**, *8*, 4576−4582.
(45) Xin, R.; Leng, Y.; Chen, J.; Zhang, Q. A Comparative Study of Calcium Phosphate Formation on Bioceramics In Vitro and In Vivo. *Biomaterials* **2005**, *26*, 6477−6486.
(46) Li, X.; Chang, J. Preparation of Bone-Like Apatite−Collagen Nanocomposites by a Biomimetic Process with Phosphorylated Collagen. *J. Biomed. Mater. Res., Part A* **2008**, *85*, 293−300.
(47) Dey, A.; Bomans, P. H. H.; Müller, F. A.; Will, J.; Frederik, P. M.; de With, G.; Sommerdijk, N. A. J. M. The Role of Prenucleation Clusters in Surface-Induced Calcium Phosphate Crystallization. *Nat. Mater.* **2010**, *9*, 1010−1014.
(48) Barrere, F.; Snel, M. M.; van Blitterswijk, C. A.; de Groot, K.; Layrolle, P. Nano-Scale Study of the Nucleation and Growth of Calcium Phosphate Coating on Titanium Implants. *Biomaterials* **2004**, *25*, 2901−2910.
(49) Turkan, U.; Guden, M. The Effect of Surface Treatment on CaP Deposition of Ti_6Al_4V Open Cell Foams in SBF Solution. *Ceram. Int.* **2010**, *36*, 1805−1816.
(50) Kim, S.; Park, C. B. Mussel-Inspired Transformation of $CaCO_3$ to Bone Minerals. *Biomaterials* **2010**, *31*, 6628−6634.
(51) Chlopek, J.; Morawska-Chochol, A.; Paluszkiewicz, C.; Jaworska, J.; Kasperczyk, J.; Dobrzyński, P. FTIR and NMR Study of Poly(Lactide-*co*-Glycolide) and Hydroxyapatite Implant Degradation under In Vivo Conditions. *Polym. Degrad. Stab.* **2009**, *94*, 1479−1485.
(52) Lin, G.; Cosimbescu, L.; Karin, N. J.; Tarasevich, B. J. Injectable and Thermosensitive PLGA-*g*-PEG Hydrogels Containing Hydroxyapatite: Preparation, Characterization and In Vitro Release Behavior. *Biomed. Mater.* **2012**, *7*, 024107−1−024107−10.
(53) Dorozhkin, S. Calcium Orthophosphates in Nature, Biology and Medicine. *Materials* **2009**, *2*, 399−498.

DOI: 10.1021/acsami.5b01440
ACS Appl. Mater. Interfaces 2015, 7, 8275−8283